Front. Phys. 13(3), 138102 (2018)
https://doi.org/10.1007/s11467-018-0758-2

RESEARCH ARTICLE

Penta-P_2X (X=C, Si) monolayers as wide-bandgap semiconductors: A first principles prediction

Mosayeb Naseri[1,†], **Shiru Lin**[2], **Jaafar Jalilian**[3], **Jinxing Gu**[2], **Zhongfang Chen**[2,‡]

[1] *Department of Physics, Kermanshah Branch, Islamic Azad University, Kermanshah, Iran*
[2] *Department of Chemistry, University of Puerto Rico, Rio Piedras Campus, San Juan, PR 00931, USA*
[3] *Young Researchers and Elite Club, Kermanshah Branch, Islamic Azad University, Kermanshah, Iran*
Corresponding authors. E-mail: †*m.naseri@iauksh.ac.ir*, ‡*zhongfangchen@gmail.com*
Received October 11, 2017; accepted December 12, 2017

By means of density functional theory computations, we predicted two novel two-dimensional (2D) nanomaterials, namely P_2X (X=C, Si) monolayers with pentagonal configurations. Their structures, stabilities, intrinsic electronic, and optical properties as well as the effect of external strain to the electronic properties have been systematically examined. Our computations showed that these P_2C and P_2Si monolayers have rather high thermodynamic, kinetic, and thermal stabilities, and are indirect semiconductors with wide bandgaps (2.76 eV and 2.69 eV, respectively) which can be tuned by an external strain. These monolayers exhibit high absorptions in the UV region, but behave as almost transparent layers for visible light in the electromagnetic spectrum. Their high stabilities and exceptional electronic and optical properties suggest them as promising candidates for future applications in UV-light shielding and antireflection layers in solar cells.

Keywords 2D materials, density functional calculations, wide bandgap semiconductors

PACS numbers 81.05.Zx, 73.22.-f

1 Introduction

Since the discovery of graphene [1], two-dimensional (2D) materials have attracted vast interest owing to their outstanding electronic and optical properties [2–9], and their potential applications in optoelectronic devices [10–17]. In recent years, many excellent 2D nanostructures have been theoretically predicted [18–25], and experimentally synthesized [26–30]. However, most 2D materials are of hexagonal lattice structures. Interestingly, in 2014, Zhang *et al.* [31] proposed a new carbon allotrope named penta-graphene. Resembling the gorgeous Cairo pentagonal tiling, the penta-graphene is composed of a pentagon network of carbon and has an intrinsic quasi-direct bandgap (3.25 eV), which is rather different from the hexagonal graphene (band gap = 0 eV). The penta-graphene also has a negative Poisson's ratio and an even better ideal strength than graphene. The advent of penta-graphene has inspired various explorations for new pentagonal 2D nanostructures. For example, Lopez–Bezanilla and Littlewood [32] proposed the 2D pentagonal C_2Si, which exhibits unusual electronic behaviors; Zhang *et al.* [33] predicted the 2D all-pentagon nitrogen-rich carbon-nitride sheet with a chemical formula of CN_2, which is insulating with a super wide bandgap of 6.53 eV; Li *et al.* [34] computationally predicted a new stable 2D inorganic material called the pentagonal B_2C monolayer, which is semiconducting with an indirect tunable bandgap of 2.28 eV.

As a group V 2D material, black phosphorene monolayer (BP) possesses a puckered structure and exceptional properties [18, 35–37]. It is semiconducting with a bandgap of 1.45 eV [35], which decreases with increasing number of layers [39–41]. Its tunable bandgap, high carrier mobility [36], and anisotropic properties endow phosphorene many promising applications, especially in electronics and optoelectronics. Other group V element 2D materials, namely, arsenene, antimonene, and bismuthene, have also been theoretically predicted [19, 42], among which arsenene and antimonene have been experimentally fabricated [29, 30, 43, 44].

Although many efforts have been carried out to design

---

*Special Topic: Inorganic Two-Dimensional Nanomaterials (Eds. Changzheng Wu & Xiaojun Wu).

pentagonal nanostructures, those works are primarily concentrated on group IV and group III elements, while pentagonal 2D materials based on group V elements have been ignored to some extent. Herein, by means of density functional theory (DFT) computations, we predicted two new pentagonal carbon/silicon phosphide monolayers, namely penta-P_2C and penta-P_2Si. We found that our newly proposed penta-P_2C and penta-P_2Si are thermodynamically, kinetically, and thermally stable, thus are promising for experimental realizations. Similar to arsenene and antimonene [19, 42], penta-P_2C and penta-P_2Si are both wide bandgap semiconductors with indirect bandgaps of 2.76 eV and 2.69 eV, respectively, and their bandgaps can be tuned by external strains. Furthermore, the optical properties of penta-P_2C and penta-P_2Si are rather superior, and have considerable absorptions in the ultraviolet region of the electromagnetic spectra but little absorption and reflection in the visible light region. These unique electronic and optical properties endow penta-P_2C and P_2Si monolayers the potential for nanoelectronics and optoelectronics, especially in UV-light shielding, and as antireflection layers in solar cells.

2 Computational methods and details

Our DFT computations for geometry optimizations and electronic/optical property evaluations were performed by employing the Wien2k code [45]. The generalized gradient approximation in the form of the Perdew–Burke–Ernzerhof (PBE) exchange-correlation functional [46] was used in our calculations. To expand the Kohn–Sham wave functions, the full-potential linear-augmented plane waves plus the local orbital (FPLAPW+lo) was applied. The $10 \times 10 \times 1$ and $20 \times 20 \times 1$ k-point meshes based on the Monkhorst–Pack scheme [47] were used to sample the Brillouin zone for the geometry optimization and for the electronic/optical property calculations, respectively. The computational input parameters of $R_{MT}K_{\max} = 7$, $G_{\max} = 14$ Ry$^{1/2}$, and $l_{\max} = 10$ were used when computing the electronic and optical properties. The random phase approximation (RPA) [48] method and the Kramers–Kronig relations were employed to gain the complex dielectric function components. To avoid the interactions between neighboring layers, a vacuum layer of at least 15 Å in the non-periodic direction (z-axis) was utilized. Since the PBE method tends to underestimate the bandgap, we also computed the bandgap values and evaluated the optical properties by the hybrid HSE06 functional.

When checking for kinetic stability, the phonon dispersions were calculated by using the density functional perturbation theory (DFPT) [49] as implemented in the QUANTUM ESPRESSO package [50], where the Martin–Troullier norm-conserving pseduopotential [51] is used to treat the core electron, while the valance electrons wave functions are expanded by using an energy cutoff of 50 Ry.

For the first principles molecular dynamic (MD) simulations, the PBE functional and DNP basis set as implemented in the DMol^3 program [52, 53] were employed, and the temperature was controlled by the Nosé–Hoover method [54]. A large super cell of $3 \times 3 \times 1$ with 54 atoms was annealed at 500, 1000, and 1500 K, respectively, and each MD simulation in the NVT canonical ensemble lasted for 10 ps with a time step of 2 fs.

3 Results and discussion

3.1 Structural properties and stability of the P_2X (X=C, Si) monolayer

As mentioned above, the prediction of the penta-graphene led to the rapid proposing of some new monolayer structures with the general form of penta-Y_2X. These pentagonal structures have been obtained by replacing the four sp^3- and two sp^2-carbon atoms in the penta-graphene unit cell with X and Y atoms, respectively. In penta-P_2C (P_2Si), each carbon (silicon) atom binds to four neighboring phosphorus atoms, while each phosphorus atom is shared by one phosphorus and two carbon (silicon) atoms (Fig. 1). The optimized lattice parameters of P_2C (P_2Si) are $a = b = 4.10$ Å (4.88 Å), while the bond angles are $\alpha = 101°$ (98°), $\beta = 112°$ (111°), and $\gamma = 99°$ (105°). It is noteworthy that the P atoms are buckled in two different atomic planes, 1.61 Å (1.86 Å) above and below the C (Si) atomic plane, respectively. In the P_2C (P_2Si) monolayer, the P-C (P-Si) and P-P (P-P) bond lengths are 1.88 (2.29), and 2.28 (2.25) Å, respectively. Compared with some recently predicted pentagonal structures (Table 1), P_2C and P_2Si have the similar unit cell size to C_2Si, but larger than

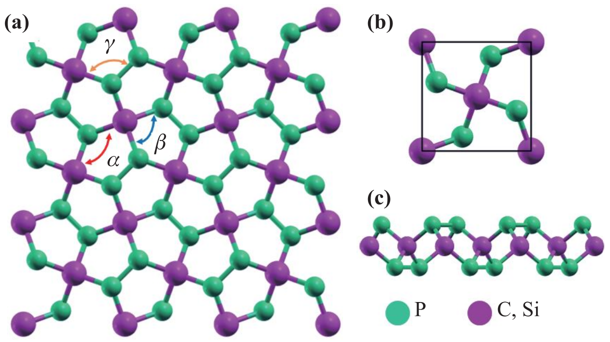

Fig. 1 **(a)** Top view, **(b)** unit cell, and **(c)** side views of the optimized structure of P_2X (X=C and Si). The pink and blue atoms represent phosphorus and X atoms (carbon and silicon), respectively.

Table 1 Structural properties of penta-P_2X (X=C, Si) and other pentagonal structures from previous work.

	P_2C	P_2Si	Penta-graphene [29]	C_2Si [30]	N_2C [31]	B_2C [32]
a, b (Å)	4.10	4.88	3.64	4.41	4.05	3.93
$X-Y$ (Å)	1.88	2.28	1.55	1.91	1.73	1.58
$Y-Y$ (Å)	2.29	2.25	1.34	1.36	1.44	1.72
Δ (Å)	2.32	2.73	1.20	1.30	1.24	1.08

penta-graphene, B_2C, and N_2C. Compared with other penta-structures in Table 1, P_2C and P_2Si have more than 1.00 Å larger thickness (Δ). All these structural features can be easily understood by the rather large sizes of P and Si atoms.

3.2 Thermodynamic, dynamic, and thermal stabilities

First, we examined the thermodynamic stability by calculating their cohesive energy (E_{coh}), which is defined as

$$E_{\mathrm{coh}} = (4E_{(\mathrm{P})} + 2E_{\mathrm{C(Si)}} - E_{\mathrm{P_2C(Si)}})/6,$$

where, $E_{\mathrm{P_2C(Si)}}$, $E_{\mathrm{C(Si)}}$, and $E_{(\mathrm{P})}$ are the total energies of the penta-P_2C(Si) unit cell, single C(Si) atom, and single P atom, respectively. According to this definition, a more positive E_{coh} value indicates a better thermodynamic stability of the structure. Based on our calculations, the cohesive energies of P_2C and P_2Si monolayers are 4.68 eV/atom and 3.94 eV/atom, respectively. In comparison, the cohesive energies for graphene [55], T-carbon [56, 57], silicene [56], and phosphorene [35–37, 57] at the same theoretical level are 7.97, 6.67, 3.94, and 3.44 eV/atom, respectively. Although the relative stability of different materials with varied compositions cannot be determined directly by their cohesive energies, the relatively high cohesive energies of penta-P_2C and P_2Si monolayers are reliable evidences for their strong intralayer bonding interactions. Based on these cohesive energies, we can further evaluate the energy changes in the following hypothetical reactions:

2 Phosphorene + Graphene → P_2C monolayer H = 0.81 eV (per P_2C unit),

2 Phosphorene + T-Carbon → P_2C monolayer H = −0.49 eV (per P_2C unit),

2 Phosphorene + Silicene → P_2Si monolayer H = −1.00 eV (per P_2Si unit).

Interestingly, the P_2Si monolayer is energetically more favorable than the elemental monolayers. Although the reaction leading to the P_2C monolayer is endothermic when graphene and phosphorene are used as reactants, it is exothermic when the highly strained T-carbon, which was recently predicted and experimentally achieved [56, 57], is utilized as the reference. Thus, both P_2X and P_2Si have reasonable thermodynamic stabilities.

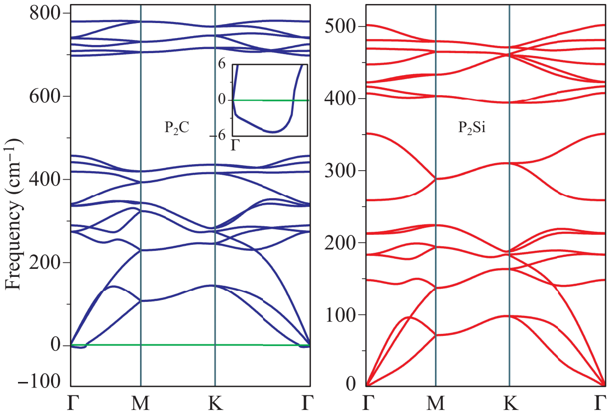

Fig. 2 Phonon dispersions of the fully optimized penta-P_2C and P_2Si monolayers. There is an insignificant imaginary mode (−5 cm^{-1} at the Γ point) for P_2C, while no imaginary mode is available for P_2Si.

Next, we investigated the kinetic stability of the penta-P_2C and P_2Si monolayers by computing their phonon dispersions. The absence of imaginary modes in the entire Brillouin zone (Fig. 2) confirms that the P_2C and P_2Si monolayers are kinetically stable. It is noteworthy that the highest frequencies for P_2C and P_2Si monolayers are 780 cm^{-1} and 500 cm^{-1}, respectively, which is higher or comparable to the highest frequency for phosphorene (440 cm^{-1}) [60], silicene (580 cm^{-1}) [61], and MoS_2 (473 cm^{-1}) [62]. The high-value frequencies in the phonon dispersion illustrate that the C/Si-P and P-P bonds are rather robust.

Third, we assessed the thermal stability of the newly predicted structures by performing first-principles molecular dynamics (FPMD) simulations. We carried out three individual MD simulations for the monolayers at temperatures of 500, 1000, and 1500 K using the 3×3×1 supercells (Fig. 3). The penta-P_2C monolayer does not collapse throughout the 10 *ps* MD simulation up to 1000 K, while the penta-P_2Si network is well retained at 1500 K. However, at 1500 (2000) K, the monolayer structure of penta-P_2C (P_2Si) is severely destroyed. The results above reveal that the penta-P_2C (P_2Si) monolayer has very good thermal stability and can maintain its structural integrity in a high-temperature environment.

The results above revealed that penta-P_2C and P_2Si monolayers have high thermodynamic, kinetic, and thermal stabilities; thus, they are feasible for experimental realizations, and are promising for applications in high temperatures.

3.3 Electronic properties

To investigate the electronic properties of penta-P_2C (P_2Si) monolayers, we first computed their band struc-

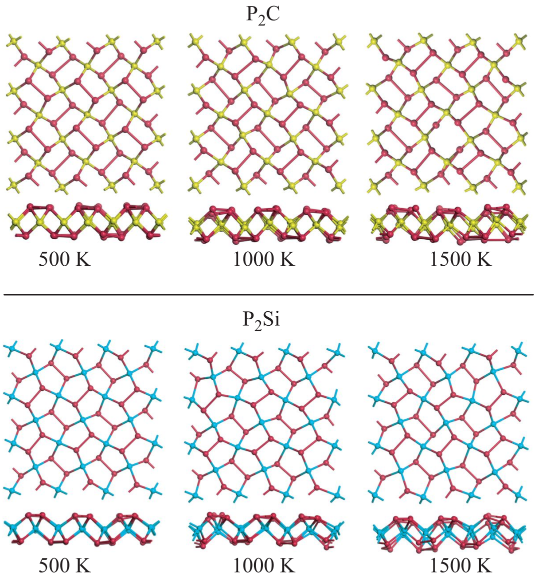

Fig. 3 Top and side views of P_2C (upper row) and P_2Si (lower row) monolayers at the end of the 10 ps MD simulations at 500, 1000, and 1500 K.

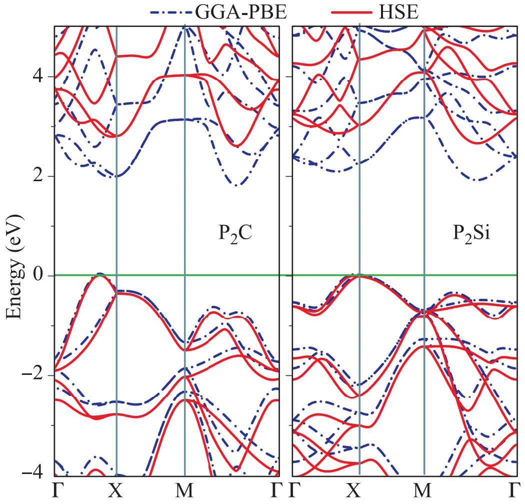

Fig. 4 Band structures of penta-P_2C (left) and P_2Si (right) by PBE (blue dash-dot lines) and HSE06 functional (red solid lines).

tures and density of states (Figs. 4 and 5) at the PBE level of theory. Both penta-P_2C and P_2Si monolayers exhibit semiconducting nature with indirect bandgaps of 1.90 eV and 1.80 eV, respectively. For the P_2C monolayer, the valence band maximum (VBM) is located between the Γ and X points, while the conduction band minimum (CBM) is between the M and Γ points. For the P_2Si monolayer, the VBM is located at the X point, and the CBM is located between the Γ and M points. The analysis of the partial density of states of these two monolayers (Fig. 5) revealed that both the VBM and CBM for penta-P_2C are primarily contributed by C-2p and P-3p orbitals, while those for penta-P_2Si are dominated by P-3p and Si-3p orbitals.

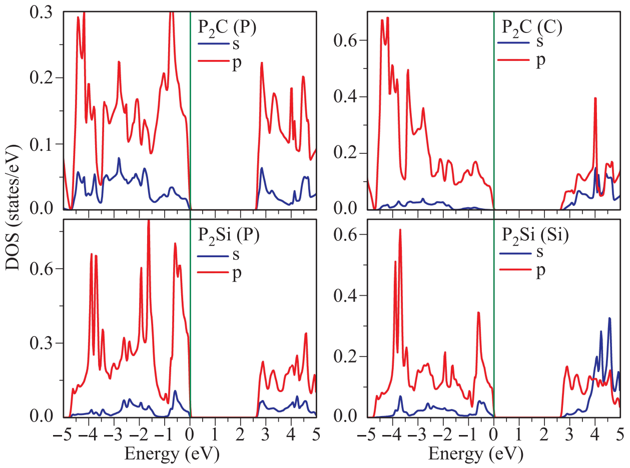

Fig. 5 Partial density of state of penta-P_2C (above) and P_2Si (below) by the HSE06 functional.

Since the GGA-PBE method tends to underestimate bandgaps, we recalculated the band gaps by the Heyd–Scuseria–Ernzerhof (HSE06) hybrid functional [63] (Fig. 4), which typically gives more reliable electronic and optical properties [64]. At the HSE06 level of theory, P_2C and P_2Si monolayers have indirect bandgaps of 2.76 eV and 2.69 eV, respectively, which are close to those of arsenene and antimonene (2.28 eV and 2.49 eV, respectively; indirect bandgap) at the same theoretical level [19, 40]. Thus, both penta-P_2C and P_2Si monolayers are indirect wide bandgap semiconductors, which are promising for blue- and UV-light-emitting diodes (LEDs) and photodetectors.

It is well known that the electronic properties of materials can be engineered by applying external strains. To obtain a deeper insight into the electronic properties of the penta-P_2C (P_2Si) monolayers, we computed their geometric structures and bandgaps under biaxial strains (Fig. 6). The variation in the lattice constants under strains are defined as $a_s = a_0(1 + \mu)$, where a_0 is the equilibrium lattice constants at 0% strain. The μ values are $\mu = 0\%$, $\pm 2\%$, $\pm 4\%$, and $\pm 6\%$. The band structures of penta-P_2C and P_2Si under various strains are presented in Figs. A1(a) and (b), respectively (see Supporting information).

The GGA-PBE and HSE06 functionals predict the same trend for the bandgap variation in the penta-P_2C and P_2Si monolayers versus external strain: the band gap increases with increasing tensile strains, and decreases upon compression. The bandgap of the penta-P_2C monolayer linearly correlates with the compressive/tensile strain. Specifically, its gap increases by 10% with 6% tensile strain, and decreases by 22% under

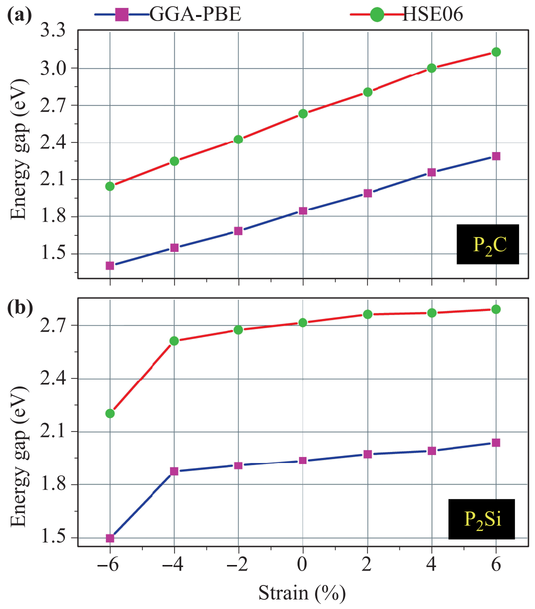

Fig. 6 Bandgaps of penta-P_2C and P_2Si monolayers as a function of the biaxial strains (PBE and HSE06 functional).

6% compression strain according to the HSE functional. The linear dependence between the bandgap and external strain also exists for the penta-P_2Si monolayer from the 4% compression strain to 6% tensile strain, but the gap merely increases approximately 3% under 6% tensile strain, and the linearity breaks down at 6% compression strain for which the bandgap drops significantly to 2.2 eV, or by ca. 19% (HSE result). Thus, the bandgap dependence on the external strain is much less pronounced for the penta-P_2Si monolayer.

3.4 Optical properties

The wide band structures of the penta-P_2C and P_2Si monolayers indicate their potential applications in UV-light shielding and other wide-gap-semiconductor devices. Thus, we investigated the optical properties of the penta-P_2C and P_2Si monolayers by calculating the complex dielectric constants $\varepsilon(\omega)=\varepsilon_1(\omega)+\mathrm{i}\varepsilon_2(\omega)$ at a given frequency using the HSE06 hybrid functional, in which ε_1 and ε_2 refer to the real and imaginary parts of the complex dielectric function, respectively. The positive value of $\varepsilon_1(\omega)$ reflects the light absorption at a given frequency ω. The imaginary component of the dielectric function is identified through the random phase approximation (RPA), which takes the interband optical transitions between the occupied and unoccupied electron states into account.

$$\varepsilon^{(2)}_{\alpha\beta}(\omega)=\frac{4\pi^2e^2}{\Omega}\lim_{q\to0}\frac{1}{q^2}\sum_{c,v,\boldsymbol{k}}2w_{\boldsymbol{k}}\delta(\varepsilon_{c\boldsymbol{k}}-\varepsilon_{v\boldsymbol{k}}-\omega)$$
$$\times\langle u_{c\boldsymbol{k}+e_\alpha\boldsymbol{q}}|u_{v\boldsymbol{k}}\rangle\langle u_{c\boldsymbol{k}+e_\beta\boldsymbol{q}}|u_{v\boldsymbol{k}}\rangle^*,$$

where the indices c and v denote the conduction and valence band states, respectively. $u_{c\boldsymbol{k}}$ to the cell periodic part of the orbitals at the k-point.

Using the HSE06 functional, we computed the optical absorption as well as the reflectivity spectrum of our newly predicted monolayers for photon energy along the$x-y$ $(E//x)$ plane and z-directions $(E//z)$ (Fig. 7). Both monolayers present almost zero absorption and very low reflection (about 3%) in the visible light range. Interestingly, they have not only considerable absorption in the ultra-violet range of the electromagnetic spectrum, but also exhibit relatively high reflectivity in this region. These unique optical properties endow penta-P_2C and P_2Si monolayers as potential applications in UV-light shielding, and as antireflection layers in solar cells.

4 Conclusions

By means of DFT computations, we predicted two pentagonal 2D materials, namely penta-P_2C and P_2Si monolayers. Both monolayers have good thermodynamic, kinetic, and thermal stabilities, which render them feasible to be realized experimentally and promising for applications at high temperatures. Both penta-P_2C and P_2Si monolayers are semiconductors with indirect wide bandgap of 2.76 eV and 2.69 eV (HSE06), respectively, and their bandgaps can be effectively tuned under external strains. Moreover, both monolayers exhibit decent absorptions in the UV region, and behave as almost transparent layers. These excellent electronic and optical properties render penta-P_2C and penta-P_2Si monolayers promising candidates for applications in the new generation of nano-optoelectronics, especially in UV light shielding, and as antireflection layers in solar cells.

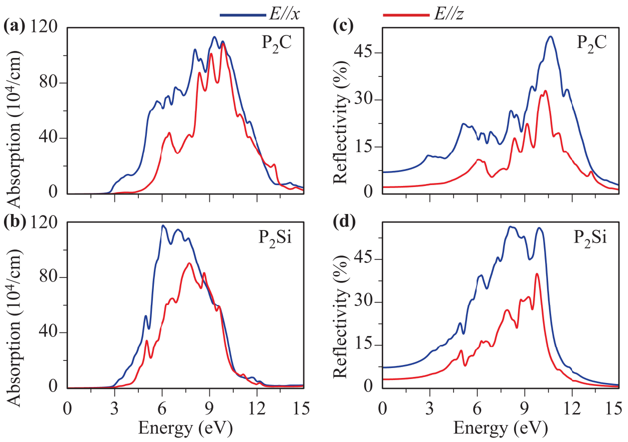

Fig. 7 The optical absorptions **(a, b)** and the reflectivity spectra **(c, d)** for photon energy along the x–y $(E//x)$ plane and z-directions $(E//z)$ of the penta-P_2C and P_2Si monolayers.

Acknowledgements This work was supported by the Kermanshah Branch, Islamic Azad University, Kermanshah, Iran. M. Naseri would like to thank Soheila Gholipour, Yasna Naseri, and Viana Naseri for their interests in this work.

Appendix A Supporting information

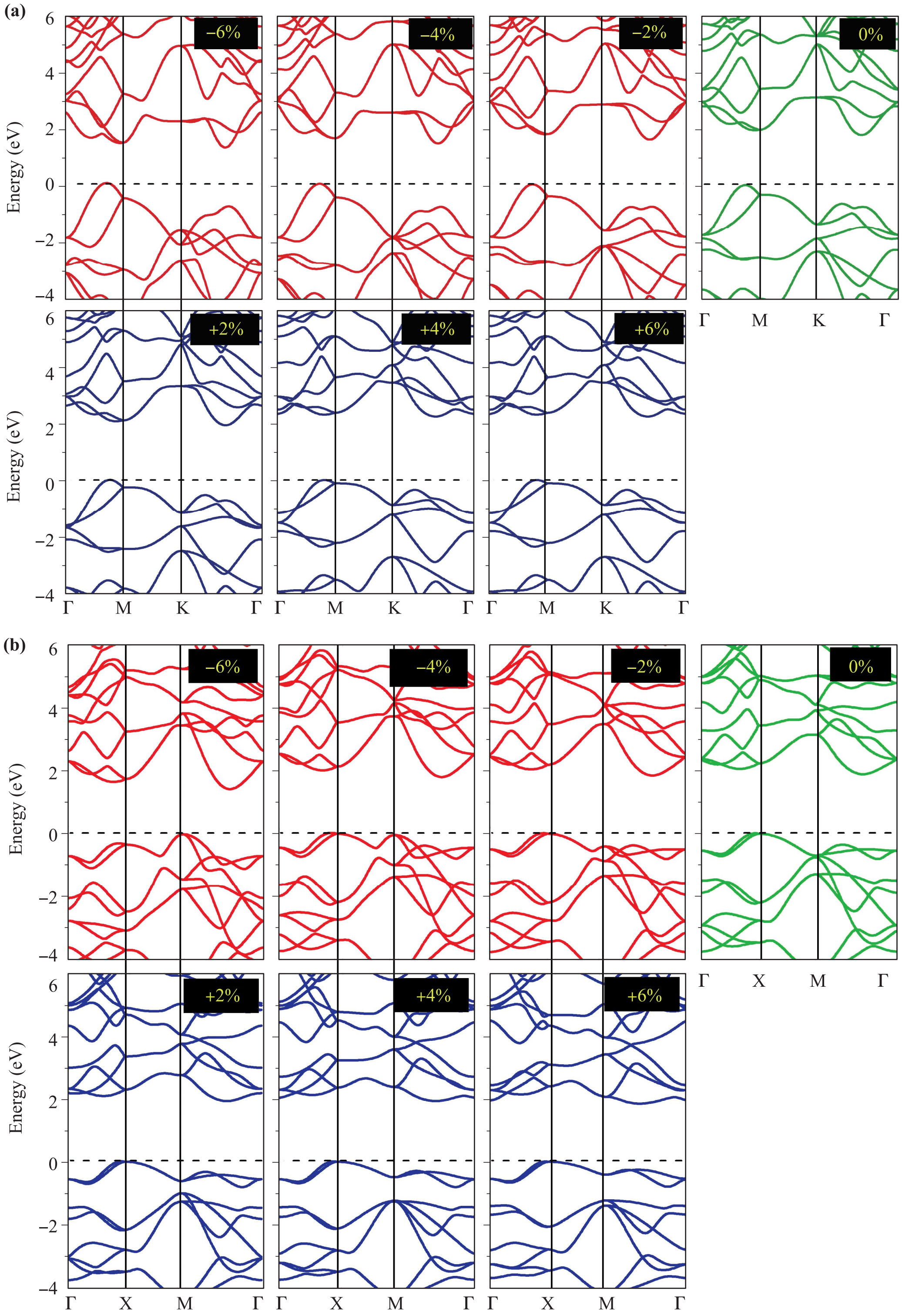

Fig. A1 The band structures of penta-P_2C **(a)** and P_2Si **(b)** versus various strains.

References and notes

1. K. S. Novoselov, A. K. Geim, S. V. Morozov, D. Jiang, Y. Zhang, S. V. Dubonos, I. V. Grigorieva, and A. A. Firsov, Electric field effect in atomically thin carbon films, *Science* 306(5696), 666 (2004)
2. Q. Tang and Z. Zhou, Graphene-analogous low-dimensional materials, *Prog. Mater. Sci.* 58(8), 1244 (2013)
3. J. J. Zhao, H. S. Liu, Z. M. Yu, R. G. Quhe, S. Zhou, Y. Y. Wang, C. C. Liu, H. X. Zhong, N. N. Han, J. Lu, Y. G. Yao, and K. H. Wu, Rise of silicene: A competitive 2D material, *Prog. Mater. Sci.* 83, 24 (2016)
4. K. S. Novoselov, A. Mishchenko, A. Carvalho, and A. H. Castro Neto, 2D materials and van der Waals heterostructures, *Science* 353(6298), aac9439 (2016)
5. S. Balendhran, S. Walia, H. Nili, S. Sriram, and M. Bhaskaran, Elemental analogues of graphene: Silicene, germanene, stanene, and phosphorene, *Small* 11(6), 640 (2015)
6. M. Xu, T. Liang, M. Shi, and H. Chen, Graphene-like two-dimensional materials, *Chem. Rev.* 113(5), 3766 (2013)
7. S. Z. Butler, S. M. Hollen, L. Cao, Y. Cui, J. A. Gupta, H. R. Gutierrez, T. F. Heinz, S. S. Hong, J. Huang, A. F. Ismach, E. Johnston-Halperin, M. Kuno, V. V. Plashnitsa, R. D. Robinson, R. S. Ruoff, S. Salahuddin, J. Shan, L. Shi, M. G. Spencer, M. Terrones, W. Windl, and J. E. Goldberger, Progress, challenges, and opportunities in two-dimensional materials beyond graphene, *ACS Nano* 7(4), 2898 (2013)
8. A. Molle, J. Goldberger, M. Houssa, Y. Xu, S. C. Zhang, and D. Akinwande, Buckled two-dimensional Xene sheets, *Nat. Mater.* 16(2), 163 (2017)
9. G. G. Guzmán-Verri and L. C. Lew Yan Voon, Electronic structure of silicon-based nanostructures, *Phys. Rev. B* 76(7), 075131 (2007)
10. X. Yu, S. Zhang, H. Zeng, and Q. J. Wang, Lateral black phosphorene P–N junctions formed via chemical doping for high performance near-infrared photodetector, *Nano Energy* 25, 34 (2016)
11. M. Xie, S. Zhang, B. Cai, Y. Huang, Y. Zou, B. Guo, Y. Gu, and H. Zeng, A promising two-dimensional solar cell donor: Black arsenic–phosphorus monolayer with 1.54 eV direct bandgap and mobility exceeding 14000 $\mathrm{cm}^2\cdot\mathrm{V}^{-1}\cdot\mathrm{s}^{-1}$, *Nano Energy* 28, 433 (2016)
12. J. Yang, Y. L. Jiang, L. J. Li, E. Muhire, and M. Z. Gao, High-performance photodetectors and enhanced photocatalysts of two-dimensional $\mathrm{TiO_2}$ nanosheets under UV light excitation, *Nanoscale* 8(15), 8170 (2016)
13. P. K. Kanaujia, and G. V. Prakash, Laser-induced microstructuring of two-dimensional layered inorganic–organic perovskites, *Phys. Chem. Chem. Phys.* 18(14), 9666 (2016)
14. G. Qin, Z. Qin, W. Z. Fang, L. C. Zhang, S. Y. Yue, Q. B. Yan, M. Hu, and G. Su, Diverse anisotropy of phonon transport in two-dimensional group Iv–Vi compounds: A comparative study, *Nanoscale* 8(21), 11306 (2016)
15. Y. Yang, S. Umrao, S. Lai, and S. Lee, Large-area highly conductive transparent two-dimensional $\mathrm{Ti_2CT}_x$ film, *J. Phys. Chem. Lett.* 8(4), 859 (2017)
16. Z. Tan, Y. Wu, H. Hong, J. Yin, J. Zhang, L. Lin, M. Wang, X. Sun, L. Sun, Y. Huang, K. Liu, Z. Liu, and H. Peng, Two-dimensional $\mathrm{(C_4H_9NH_3)_2PbBr4}$ perovskite crystals for high-performance photodetector, *J. Am. Chem. Soc.* 138(51), 16612 (2016)
17. D. Yin, J. Feng, N. R. Jiang, R. Ma, Y. F. Liu, and H. B. Sun, Two-dimensional stretchable organic light-emitting devices with high efficiency, *ACS Appl. Mater. Interfaces* 8(45), 31166 (2016)
18. Y. Jing, X. Zhang, and Z. Zhou, Phosphorene: What can we know from computations? *Wiley Interdiscip. Rev.: Comput. Mol. Sci.* 6(1), 5 (2016)
19. S. Zhang, M. Xie, F. Li, Z. Yan, Y. Li, E. Kan, W. Liu, Z. Chen, and H. Zeng, Semiconducting group 15 monolayers: A broad range of band gaps and high carrier mobilities, *Angew. Chem. Int. Ed.* 55(5), 1666 (2016)
20. L. Chen, C. C. Liu, B. Feng, X. He, P. Cheng, Z. Ding, S. Meng, Y. Yao, and K. Wu, Evidence for Dirac fermions in a honeycomb lattice based on silicon, *Phys. Rev. Lett.* 109(5), 056804 (2012)
21. K. Shehzad, Y. Xu, C. Gao, and X. Duan, Three-dimensional macro-structures of two-dimensional nanomaterials, *Chem. Soc. Rev.* 45(20), 5541 (2016)
22. P. Z. Tang, P. C. Chen, W. D. Cao, H. Q. Huang, S. Cahangirov, L. D. Xian, Y. Xu, S. C. Zhang, W. H. Duan, and A. Rubio, Stable two-dimensional dumbbell stanene: A quantum spin Hall insulator, *Phys. Rev. B* 90(12), 121408 (2014)
23. S. Rachel and M. Ezawa, Giant magnetoresistance and perfect spin filter in silicene, germanene, and stanene, *Phys. Rev. B* 89(19), 195303 (2014)
24. Q. Tang, Z. Zhou, and Z. Chen, Innovation and discovery of graphene-like materials via density-functional theory computations, *Wiley Interdiscip. Rev.: Comput. Mol. Sci.* 5(5), 360 (2015)
25. X. Zhang, Z. Zhang, X. Zhao, D. Wu, and Z. Zhou, MnBx monolayers with quasi-planar hypercoordinate Mn atoms and unique magnetic and mechanical properties, *FlatChem* 4, 42 (2017)
26. L. Li, S. Z. Lu, J. Pan, Z. Qin, Y. Q. Wang, Y. Wang, G. Y. Cao, S. Du, and H. J. Gao, Buckled germanene formation on Pt(111), *Adv. Mater.* 26(28), 4820 (2014)
27. F. F. Zhu, W. J. Chen, Y. Xu, C. L. Gao, D. D. Guan, C. H. Liu, D. Qian, S. C. Zhang, and J. F. Jia, Epitaxial growth of two-dimensional stanene, *Nat. Mater.* 14(10), 1020 (2015)

28. H. S. Tsai, S. W. Wang, C. H. Hsiao, C. W. Chen, H. Ouyang, Y. L. Chueh, H. C. Kuo, and J. H. Liang, Direct synthesis and practical bandgap estimation of multilayer arsenene nanoribbons, *Chem. Mater.* 28(2), 425 (2016)
29. H. S. Tsai, C. W. Chen, C. H. Hsiao, H. Ouyang, and J. H. Liang, The advent of multilayer antimonene nanoribbons with room temperature orange light emission, *Chem. Commun.* 52(54), 8409 (2016)
30. J. Ji, X. Song, J. Liu, Z. Yan, C. Huo, S. Zhang, M. Su, L. Liao, W. Wang, Z. Ni, Y. Hao, and H. Zeng, Two-dimensional antimonene single crystals grown by van Der Waals epitaxy, *Nat. Commun.* 7, 13352 (2016)
31. S. Zhang, J. Zhou, Q. Wang, X. Chen, Y. Kawazoe, and P. Jena, Penta-graphene: A new carbon allotrope, *Proc. Natl. Acad. Sci. USA* 112(8), 2372 (2015)
32. A. Lopez-Bezanilla, and P. B. Littlewood, S–P-band inversion in a novel two-dimensional material, *J. Phys. Chem. C* 119(33), 19469 (2015)
33. S. Zhang, J. Zhou, Q. Wang, and P. Jena, Beyond graphitic carbon nitride: Nitrogen-rich penta-CN_2 sheet, *J. Phys. Chem. C* 120(7), 3993 (2016)
34. F. Li, K. Tu, H. Zhang, and Z. Chen, Flexible structural and electronic properties of a pentagonal B_2C monolayer via external strain: A computational investigation, *Phys. Chem. Chem. Phys.* 17(37), 24151 (2015)
35. H. Liu, A. T. Neal, Z. Zhu, Z. Luo, X. Xu, D. Tománek, and P. D. Ye, Phosphorene: An unexplored 2D semiconductor with a high hole mobility, *ACS Nano* 8(4), 4033 (2014)
36. L. Li, Y. Yu, G. J. Ye, Q. Ge, X. Ou, H. Wu, D. Feng, X. H. Chen, and Y. Zhang, Black phosphorus field-effect transistors, *Nat. Nanotechnol.* 9(5), 372 (2014)
37. R. W. Keyes, The electrical properties of black phosphorus, *Phys. Rev.* 92(3), 580 (1953)
38. Y. Takao, H. Asahina, and A. Morita, Electronic structure of black phosphorus in tight binding approach, *J. Phys. Soc. Jpn.* 50(10), 3362 (1981)
39. D. Warschauer, Electrical and optical properties of crystalline black phosphorus, *J. Appl. Phys.* 34(7), 1853 (1963)
40. S. Narita, Y. Akahama, Y. Tsukiyama, K. Muro, S. Mori, S. Endo, M. Taniguchi, M. Seki, S. Suga, A. Mikuni, and H. Kanzaki, Electrical and optical properties of black phosphorus single crystals, *Physica* $B + C$ 117–118, 422 (1983)
41. Y. Maruyama, S. Suzuki, K. Kobayashi, and S. Tanuma, Synthesis and some properties of black phosphorus single crystals, *Physica* $B + C$ 105(1–3), 99 (1981)
42. S. Zhang, Z. Yan, Y. Li, Z. Chen, and H. Zeng, Atomically thin arsenene and antimonene: Semimetal-semiconductor and indirect-direct band-gap transitions, *Angew. Chem. Int. Ed.* 54(10), 3112 (2015)
43. P. Ares, F. Aguilar-Galindo, D. Rodriguez-San-Miguel, D. A. Aldave, S. Diaz-Tendero, M. Alcami, F. Martin, J. Gomez-Herrero, and F. Zamora, Mechanical isolation of highly stable antimonene under ambient conditions, *Adv. Mater.* 28(30), 6332 (2016)
44. C. Gibaja, D. Rodriguez-San-Miguel, P. Ares, J. Gomez-Herrero, M. Varela, R. Gillen, J. Maultzsch, F. Hauke, A. Hirsch, G. Abellan, and F. Zamora, Few-layer antimonene by liquid-phase exfoliation, *Angew. Chem. Int. Ed.* 55(46), 14345 (2016)
45. P. Blaha, K. Schwarz, G. Madsen, D. Kvasnicka, J. Luitz, and K. Schwarz, An augmented PlaneWave+ Local Orbitals Program for calculating crystal properties revised edition WIEN2k 13.1 (release 06/26/2013)
46. J. P. Perdew, K. Burke, and M. Ernzerhof, Generalized gradient approximation made simple, *Phys. Rev. Lett.* 77(18), 3865 (1996)
47. H. J. Monkhorst and J. D. Pack, Special points for Brillouin-zone integrations, *Phys. Rev. B* 13(12), 5188 (1976)
48. R. Abt, C. Ambrosch-Draxl, and P. Knoll, Optical response of high temperature superconductors by full potential LAPW band structure calculations, *Physica B* 194–196, 1451 (1994)
49. X. Gonze and C. Lee, Dynamical matrices, born effective charges, dielectric permittivity tensors, and interatomic force constants from density-functional perturbation theory, *Phys. Rev. B* 55(16), 10355 (1997)
50. P. Giannozzi, S. Baroni, N. Bonini, M. Calandra, R. Car, et al., Quantum espresso: A modular and open-source software project for quantum simulations of materials, *J. Phys.: Condens. Matter* 21(39), 395502 (2009)
51. N. Troullier and J. L. Martins, Efficient pseudopotentials for plane-wave calculations, *Phys. Rev. B* 43(3), 1993 (1991)
52. B. Delley, An all-electron numerical-method for solving the local density functional for polyatomic-molecules, *J. Chem. Phys.* 92(1), 508 (1990)
53. B. Delley, From molecules to solids with the Dmol^3 approach, *J. Chem. Phys.* 113(18), 7756 (2000)
54. G. J. Martyna, M. L. Klein, and M. Tuckerman, Nosé–Hoover chains: The canonical ensemble via continuous dynamics, *J. Chem. Phys.* 97(4), 2635 (1992)
55. H. Shin, S. Kang, J. Koo, H. Lee, J. Kim, and Y. Kwon, Cohesion energetics of carbon allotropes: Quantum Monte Carlo study, *J. Chem. Phys.* 140(11), 114702 (2014)
56. X. L. Sheng, Q. B. Yan, F. Ye, Q. R. Zheng, and G. Su, T-carbon: A novel carbon allotrope, *Phys. Rev. Lett.* 106(15), 155703 (2011)
57. J. Y. Zhang, R. Wang, X. Zhu, A. Pan, C. Han, X. Li, D. Zhao, C. Ma, W. Wang, H. Su, and C. Niu, Pseudo-topotactic conversion of carbon nanotubes to T-carbon nanowires under picosecond laser irradiation in methanol, *Nat. Commun.* 8(1), 683 (2017)

58. N. Drummond, V. Zolyomi, and V. I. Fal'ko, Electrically tunable band gap in silicene, *Phys. Rev. B* 85(7), 075423 (2012)
59. Y. Wang, F. Li, Y. Li, and Z. Chen, Semi-metallic Be_5C_2 monolayer global minimum with quasi-planar pentacoordinate carbons and negative Poisson's ratio, *Nat. Commun.* 7, 11488 (2016)
60. G. Qin, Q. B. Yan, Z. Qin, S. Y. Yue, M. Hu, and G. Su, Anisotropic intrinsic lattice thermal conductivity of phosphorene from first principles, *Phys. Chem. Chem. Phys.* 17(7), 4854 (2015)
61. L. F. Huang, P. L. Gong, and Z. Zeng, Phonon properties, thermal expansion, and thermomechanics of silicene and germanene, *Phys. Rev. B* 91(20), 205433 (2015)
62. Molina-Sánchez and L. Wirtz, Phonons in single-layer and few-layer MoS_2 and WS_2, *Phys. Rev. B* 84(15), 155413 (2011)
63. J. Heyd, G. E. Scuseria, and M. Ernzerhof, Hybrid functionals based on a screened coulomb potential, *J. Chem. Phys.* 118(18), 8207 (2003)
64. H. Zhang, D. Wu, Q. Tang, L. Liu, and Z. Zhou, Zno–Gan heterostructured nanosheets for solar energy harvesting: Computational studies based on hybrid density functional theory, *J. Mater. Chem. A Mater. Energy Sustain.* 1(6), 2231 (2013)